J. Braz. Chem. Soc., Vol. 7, No. 6, 471-483, 1996.
Printed in Brazil.

0103 – 5053 $6.00 + 0.00

Article

Acoustic Phonons in Superlattices

V. Lemos[a], *O. Pilla*[b], *and M. Montagna*[b]

[a]*Instituto de Física "Gleb Wataghin" Universidade Estadual de Campinas, UNICAMP, 13083-970 Campinas - SP, Brazil*

[b]*Istituto Nazionale di Fisica della Materia, Dipartimento di Fisica, Universitá di Trento, I-38050, Povo - Trento, Italy*

Received: June 17, 1996

Neste trabalho, resultados de algumas publicações recentes em espalhamento por fonons acústicos em super redes, são discutidos. Novas informações obtidas através de espectroscopia Raman em superredes fabricadas com elementos do grupo IV são também apresentadas. Os dados revelam linhas entre os picos correspondentes aos fonons dobrados, dentro dos gaps acústicos. Nós mostramos que as freqüências dos modos do gap são características de um sistema de duas camadas, considerado como a cela unitária da super rede. Os espectros de superredes opacas são bandas largas sobre as quais aparecem depressões bastante pronunciadas. Absorção é responsável pelo alargamento que, por sua vez, permite observar as depressões, as quais são estruturas típicas dos gaps acústicos. A estrutura fina no espectro de super redes de período curto, é comparada com a densidade de estados. É mostrado neste trabalho que a estrutura fina é conseqüência da dimensão finita da superrede. O cálculo do espalhamento Raman usado para o ajuste das experiências serviu de base para a interpretação física dos resultados.

Some recent publications related to acoustic phonon scattering in superlattices are reviewed. New information on the Raman spectroscopy of diamond-like constituent superlattices is also presented. The data reveal sharp lines appearing between those of folded phonon doublets inside the acoustic gaps. We show that the gap mode frequencies are characteristic of the bilayer system, taken as the unit cell of the superlattice. Spectra from highly absorbent superlattices show pronounced dips in intensity that are superimposed on the broad band scattering. Absorption is responsible for the broadening, thus revealing the dips which are typical features of acoustic gaps. The fine structure in the spectra of short-period superlattices is compared with the projected density of states. It is shown that the fine structure appears because of finite size effects. A calculation of low-frequency Raman scattering used for modeling the experimental spectra serves as base for the physical interpretation of the results.

Keywords: *Raman scattering, acoustic phonons, superlattices*

Introduction

Raman scattering by acoustic phonons in superlattices reveals peculiar features in the low frequency region of the spectra[1-4]. The subject is exciting because these features are unusual, since they appear in a frequency range where usually only the doublets of folded phonons are observed[5]. Supplementary structures in the spectra, appearing as sharp lines and secondary oscillations, have also attracted attention[6-9]. Experimental evidence of acoustic gaps has been found, but only for the internal gaps which result from the mixing of longitudinal and transverse waves[1-4]. This evidence consists of dips observed in the scattered intensity which are superimposed on the continuum at frequencies where longitudinal and transverse dispersion cross. The allowance for transverse scattering from a (001)-face of zinc blend (ZB) constituent was attributed to an in-plane component of the crystal momentum, due to interface roughness[1-3]. In the pioneering observations of such gaps, the scattering by transverse phonons was allowed in the backscattering geometry of (111)-faces of ZB materials[4]. The anomalies appeared as weak structures, due to the lack

of a continuum[4]. These are some of the reasons why there is a considerable ongoing effort to formulate a model for acoustic phonon Raman scattering in superlattices[1,10]. Earlier approaches based on the transfer matrix method (TMM) have been remarkably successful in predicting acoustic properties, in spite of inaccuracies due to the limitations of modeling ideal infinite superlattices[10]. Finite size effects were predicted in the theoretical treatments based on the TMM in Refs. 11 and 12. These articles suggests that the engineering of phonon devices, such as oscillators or filters, could soon become a reality.

The aim of this work is to review some of our recent reports on the observation and interpretation of acoustic modes in superlattices. We limit the subject to diamond-like constituent superlattices based on Si or Ge. Our discussion is restricted to four selected samples: two Si/Ge_xSi_{1-x} wide-period superlattices with varying germanium composition and period, one Ge/Ge_xSi_{1-x} wide-period superlattice with $x = 0.72$, and one Ge_5Si_5 short-period superlattice. The first three samples permitted to probe close to the mini Brillouin zone edge. A numerical calculation of the Raman scattering based on the transfer matrix method, enabled the reproduction of fine structures in the spectra[7]. By applying this treatment to evaluate the scattering, our experimental results could be fully described, including the lines occurring in the gaps between two neighboring members of folded acoustic phonon doublets.

Experimental

Overview and instrumentation

Raman scattering has been a standard technique for the study of superlattices for decades, and has more recently spread to the study of novel low dimensional systems[13,14], for which most of the necessary equipment is commercially available. The progress in the field of instrumentation is mainly due to the advances in multichannel detection systems. Details of this technique have recently been discussed in Refs. 15 and 16. This development has found widespread application in new Raman instrumentation employing short focal length spectrometers associated with notch filters, having unmatched performance in the energy range of optical phonons. However, the acoustic phonon range, a few cm^{-1} from the excitation energy, is inaccessible with this instrumentation. Considerable efforts spent in developing modern equipment for low-frequency light scattering has resulted in the design of a special double monochromator double pass, the DMDP 2000[17]. Because of its extreme resolution and straight light rejection this instrument capability is well established for the study of Brillouin and high-resolution Raman spectroscopy. Due to the high degree of experimental sophistication it is difficult to measure the full phonon spectrum, comprising both acoustic and optical ranges, in a single run.

A SOPRA DMDP 2000 was used in our measurements in a single pass configuration chosen to increase transmittance. This setting allowed a resolution between 0.23 cm^{-1} and 0.46 cm^{-1}, with a slit width of 200 μm and 300 μm, employed here for the Si-based and Ge-based samples, respectively. The Raman scattering measurements were carried out using a 90° scattering geometry, which is nearly backscattering inside the sample[18]. The excitation was either the 514.5 nm or the 496.5 nm line of an Ar ion laser with ~200 mW of output power. The incident light was polarized in the plane of incidence, and the polarization of the scattered light was not analyzed.

Sample description

The wide-period Si/Ge_xSi_{1-x} and Ge/Ge_xSi_{1-x} superlattices used in this work, each with $N = 20$ periods, were MBE-grown on a (001)-oriented substrate. Their characteristics are listed in Table 1. Samples 1 and 2 were grown on a Si substrate, and sample 3 on a Ge substrate. Layer thicknesses d_1 and d_2, as well as Ge composition x, were determined from double-crystal X-ray diffraction measurements[6]. Index 1 is used here for the single element layer, and 2 for the alloy layer. The cap layer thickness is denoted by d_c. A marked difference exists between the first two samples and the third as far as absorption is concerned. The latter is strongly absorbing, while Si-based samples have negligible absorption. Table 1 also lists a short-period MBE-grown superlattice, consisting of 145 periods of Si_n-Ge_n , with $n = 5$ monolayers. For this sample, indexes 1 and 2 refer to Si and Ge, respectively.

The Theoretical Model

The folding effect

This work is concerned with acoustic modes in superlattices and we discuss only superlattices made out of diamond-like bulk constituents. The direction of growth is assumed to be $z = [001]$, since this is the most commonly investigated case. In this direction the crystals have a much larger lattice constant than the corresponding single crystals, the new translational period being $d = d_1 + d_2$, where d_1 and d_2 are the layer thicknesses. Because of the superperiodicity, the Brillouin zone must be folded back into many branches in order to stay within the reduced zone scheme.

Table 1. Data for Si/Ge_xSi_{1-x} superlattices (samples 1 and 2), Ge/Ge_xSi_{1-x} (sample 3), and a short-period Ge_5Si_5 superlattice (sample 4).

sample	x	d_1 (nm)	d_2 (nm)
1	0.39	25.5	8.5
2	0.44	21.5	5.0
3	0.70	11.5	11.5
4		6.7	7.5

The folding discloses several new modes which can be observed using optical spectroscopy. The folding effect is illustrated in Fig. 1 for a diatomic linear chain, chosen here for the sake of simplicity. The mass relation was adopted as M = 1.5 m and the superperiod was taken as $10a$, with a being the period of the chain. The bulk-like acoustic branch is folded into 10 branches in the small zone, generating 10 acoustic modes for any wave vector in the range $0 < k < \pi/10a$. The superlattice period, d, is commonly found to be close to 10 times the mean bulk lattice parameter of constituent layer materials, $\langle a \rangle$. At this point it is worth calling attention to the fact that thick layer superlattices have a period on the order of $100\langle a \rangle$, and in this case the folding occurs at a smaller wave vector. Schematic representation of the folding of the Brillouin zone for common superlattices can be found in Ref. 19.

The scattering model

In this approach we consider the scattered intensity by a homogeneous medium, as in ordinary Brillouin scattering, which is given by the expression[20]:

$$I(\omega) \propto \left| \int \exp(-iqz) \frac{\partial u(\omega, z)}{\partial z} P(z)\, dz \right|^2 \qquad (1)$$

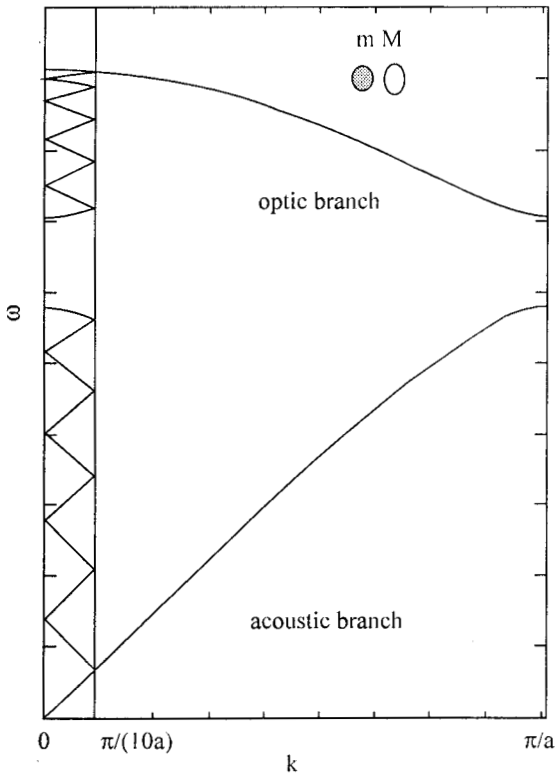

Figure 1. A linear-chain model calculation of the phonon dispersion curve for longitudinal acoustic and optic modes. The small zone illustrates the folding effect.

where q is the exchange photon wave vector magnitude, $P(z)$ is the acoustic-optic parameters, and $u(\omega, z)$ is the normalized displacement from the equilibrium position, z, for the normal mode of vibration of frequency ω. The integration is performed up to the limit of the scattering volume in the z direction. In other words, it is taken as a sum in the superlattice with the effective range determined by the decay in the electrical field due to the absorption of light. The phonon wave vector is considered to be parallel to the [001] crystalline direction, and interfaces are taken as perfect yielding decoupled modes in the backscattering configuration[21]. All the quantities appearing in (1) can be calculated if the parameters of the materials such as refraction indexes, layer thicknesses, elastic constants and sound velocities, are known. When there is some uncertainty about these we are faced with the inverse problem: to determine the values of these quantities from the Raman spectra. Actually, the parameters of the materials can be determined independently, since they are related to different aspects of the line shapes of the spectra. To pursue this idea, it is necessary to analyze in some detail the role of the three terms appearing in the integral of (1). This will be discussed separately in that follows.

Elastic continuum model

In the continuum model for the lattice vibration, the solution to the one-dimensional wave equation reads[11,12]:

$$u_j(z) = t_j \exp(ik_j z) + r_j \exp(-ik_j z) \qquad (2)$$

The index j specifies the constituent layer, t_j and r_j are the amplitudes of transmitted and reflected waves, respectively, and k_j is the wavenumber. The stress is given by:

$$S_j = C_j \left(\frac{\partial u_j}{\partial z}\right) \qquad (3)$$

with C_j specifying the elastic constants. It is convenient to introduce a matrix notation to be able to impose continuity conditions at interfaces to displacement and stress simultaneously, as follows:

$$\mathbf{V_j(z)} = \begin{bmatrix} \mathbf{u_j(z)} \\ \mathbf{S_j(z)} \end{bmatrix}; \qquad \mathbf{A_i} = \begin{bmatrix} \mathbf{t_j} \\ \mathbf{r_j} \end{bmatrix} \qquad (4)$$

Definitions (2) and (3) in the matrix notation, give:

$$V_j(z) = M_j(z)\, A_j\,, \qquad (5)$$

with

$$M_j(z) = \begin{bmatrix} exp(\mathrm{i}\,\mathbf{k}_j z) & exp(-\mathrm{i}\,\mathbf{k}_j z) \\ \mathrm{i}\omega Z_j exp(\mathrm{i}\,\mathbf{k}_j z) & -\mathrm{i}\omega Z_j exp(\mathrm{i}\,\mathbf{k}_j z) \end{bmatrix} \qquad (6)$$

where Z_j is the acoustic impedance ($\rho_j \vartheta_j$) and $\omega = k_j \vartheta_j$. Here, ρ stands for the density and ϑ for the sound velocity. In addition, the boundary conditions require that:

$$V_j[(n+1)\Delta z] = T_j[(n+1)\Delta z].V_j(n\Delta z). \quad (7)$$

The transfer matrix, T_j, is obtained from definition (5), as:

$$T_j[(n+1)\Delta z] = M_j[(n+1)\Delta z]\, M_j^{-1}(n\Delta z) \quad (8)$$

and explicitly by:

$$T_j[(n+1)\Delta z] = \begin{bmatrix} cos\alpha & \frac{1}{\omega Z_j} sin\alpha \\ -\omega Z_j sin\alpha & cos\alpha \end{bmatrix} \quad (9)$$

with $\alpha = k_j(n+1)\Delta z$

In the numerical calculation we took stress-free boundary conditions at the air-superlattice interface, which produce stationary wave solutions.

Electromagnetic wave propagation

The momentum conservation rule, $\mathbf{q} = \mathbf{k_i} - \mathbf{k_s}$,, at the long wavelength limit, allows for the approximation:

$$\mathbf{q} \sim -2\mathbf{k_i} \quad (10)$$

Here, $\mathbf{k_i}$ ($\mathbf{k_s}$) stands for the wave vector of the incident (scattered) radiation. With $\mathbf{k_0}$ being the wave vector in vacuum the magnitude of the phonon wave vector is:

$$q \sim -2nk_0 \quad (11)$$

Strict calculations of the electromagnetic propagation should be made by a transfer matrix method similar to that described above for the elastic continuum. However, the results are not greatly affected if a simplification is introduced using an effective refraction index assumed to be equal for both constituent materials as[7]:

$$\langle n \rangle = \left[\frac{(n_1^2 d_1 + n_2^2 d_2)}{d}\right]^{1/2} \quad (12)$$

It is useful to remember that this assumption is equivalent to the absence of reflections of electromagnetic waves at the interfaces. In order to allow the absorption effects to be directly included in our calculations, the complex refraction index was used. The presence of absorption allows for the line width of the Raman peaks to be properly accounted for.

The photoelastic mechanism

Far from resonance conditions, light scattering from folded acoustic phonons can be treated as a coherent sum of scattering within bulk-like layers, due to the photoelastic effect. The photoelastic coefficient can be taken as a square wave function of position, such[25]:

$$P(z) = \begin{cases} P_1 & 0 \le z \le d_1 \\ P_2 & d_1 \le z \le d \end{cases} \quad (13)$$

The role of this function is to represent the polarizability modulation due to the photoelastic coupling affecting the relative intensities of the acoustic modes in the spectra. Although the components of the photoelastic tensors have been measured for many diamond semiconductors below the absorption edge, information is lacking in the region of absorption. Also, the corresponding information for alloy bulk constituents and the effects of the superlattice on those parameters are not available. Because of this lack of information on the values of acoustic-optic coefficients, they latter are commonly taken as adjustable parameters in order to obtain the efficiency profile. This procedure was adopted here by summing up contributions from the two different layers in components A_1 and A_2, respectively, and by modulation through a relative P_1/P_2 value. As a consequence, Eq. 1 can be rewritten for a particular mode as:

$$I(\omega) \propto \left| A_1(\omega) + A_2(\omega) \frac{P_2}{P_1} \right|^2 \quad (14)$$

with

$$A_j(\omega) = \int \exp(-iq_j z) \frac{\partial u_j(\omega, z)}{\partial z} dz \qquad j = 1, 2 \quad (15)$$

The numerical calculation of (14) refers to a complete system with cap, superlattice, and substrate.

The projected density of states

The contribution of the different vibrational modes is determined by their amplitudes in the scattering volume. This can be taken into account by considering a density of states projected on a definite range of z near the surface, the projected density of states (PDOS). The PDOS can be measured by the mean square amplitude of the modes in the region of interest. We studied the problem in detail for several systems, and found that the PDOS is strongly sensitive to the structure of the superlattice. To illustrate this point we selected three examples: a short period Ge_5Si_5 superlattice, described as sample 4 in Table 1, a wide-period Si/Ge_xSi_{1-x} superlattice (sample 2 in Table 1), and another wide-period hypothetical superlattice with a structure identical to that of sample 2, except that the number of periods is N = 200.

Figure 2(a) [Fig. 2(e)] shows the dispersion relation for the short period (wide period superlattice). The dispersion curves for the large period superlattices consist of several folded branches. In contrast, the short period superlattice dispersion curve in the same frequency range is a single branch, since the first folding is expected to occur at ~67cm^{-1}. Traces 2(b), 2(c), and 2(d) are the PDOS corresponding to the Ge_5Si_5 and the Si/Ge_xSi_{1-x} (x = 0.44) superlattices, with N = 20 and N = 200 periods, respectively. Plot 2(b) is a highly structured function of ω, showing several small oscillations which are

related to the number of periods of the superlattice. Due to the finite-size effects, there are 145 oscillations per branch in the dispersion relation. In the intermediate curve, Fig. 2(c), the number of small oscillations per branch is 20. Finally, at the lower curve, Fig. 2(d), corresponding to N = 200, the 200 oscillations per branch merge into a quasi-continuum, very similar to the one that can be calculated for an ideal infinite superlattice for which the well-known Rytov relation[23] is used. It is worth mentioning that the latter curve lacks structures in the frequency ranges corresponding to the gaps in the dispersion curve of Fig. 2(e), probably due to the delta function like behavior of the peaks in the limit $N \rightarrow \infty$ [24]. In the case of the superlattice with N = 20 periods in Fig. 2(c), however, several peaks are seen inside the gap region. These features, also present in the plots of transmission coefficients[12], were interpreted in terms of layer vibrations according to a detailed description given further on. As we shall see in the examples given in a following section, the use of the PDOS, which actually does not enter into the calculation of the scattering, is important because it gives the energy position of the structures in the spectra. In this way, the structural and dynamic aspects can be discussed independent of the optical and acoustic-optical effects.

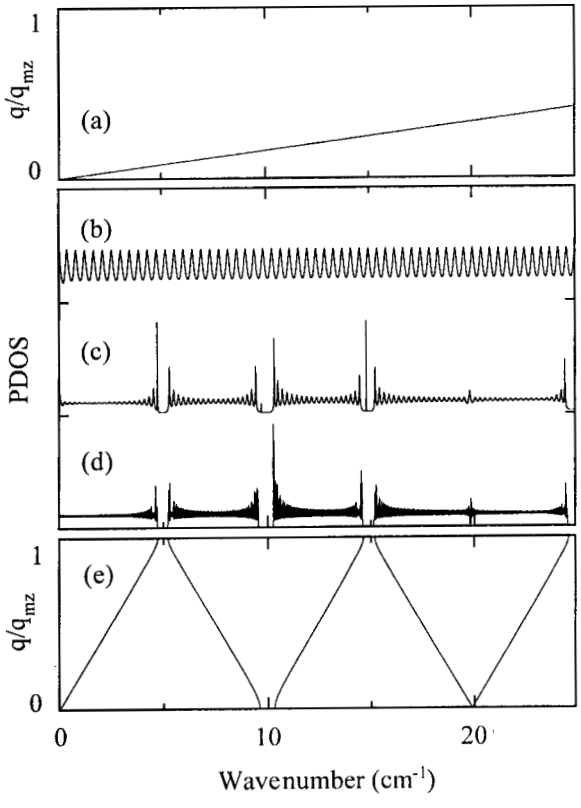

Figure 2. A dispersion relation for (a) a ∞-Si/$Ge_{0.44}Si_{0.56}$ superlattice, (b) a N = 45 period Ge5Si5 superlattice, (c) a N = 20 period Si//$Ge_{0.44}Si_{0.56}$ superlattice, and (d) the same as the latter, but for N = 200 periods.

Results and Discussion

In the previous section we commented on several effects concerning the absorption of light, periodic modulation of the density of states, and modes appearing inside the forbidden gaps. To better explain these effects we will group the results into three different subsections as follows.

Gap modes

Raman spectra of large period Si/Ge_xSi_{1-x} superlattices are presented in this section. Figure 3 displays the experimental spectra as solid curves. The upper curve in this figure was obtained using excitation with the 514.5 nm line, and the bottom curve with the 496.5 nm line. For those excitation energies, the scattered wave vectors are given by $q_a = 1.15\ q_{mz}$ and $q_b = 1.23\ q_{mz}$ respectively, with q_{mz} being the wave vector at the limit of the mini Brillouin zone. Because we are probing close to the zone edge, structures in the Raman spectra should only appear at frequencies corresponding to this wave vector. In fact, the spectra display three zone edge doublets centered at frequencies ~4 cm^{-1}, ~11 cm^{-1}, and ~19 cm^{-1}. Of interest is the doublet at ~19 cm^{-1} because of the additional line appearing at 19.3 cm^{-1}, which is just discernible in Fig. 3(a), but can be clearly seen in Fig. 3(b). This is probably due to the increased separation of the doublet on the bottom curve as a consequence of probing farther apart the zone edge. As the 19.3 cm^{-1} line is present in both spectra, it should have the same physical origin as the Raman modes. We calculated the transverse acoustic (TA) mode frequencies and did not

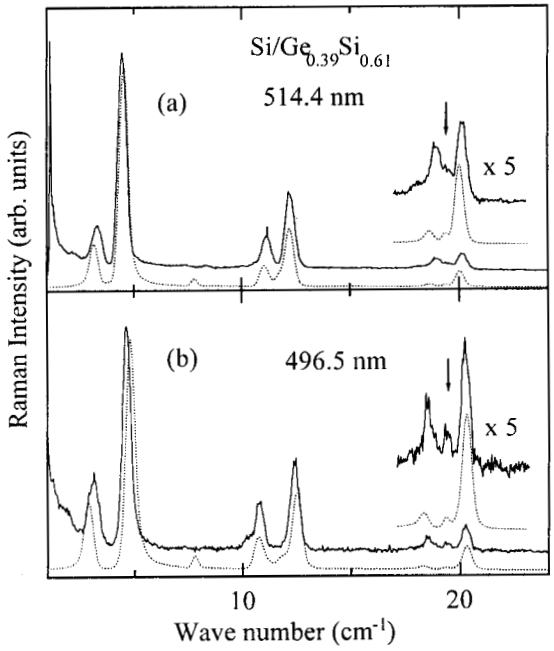

Figure 3. Measured (solid line) and calculated (dots) Raman spectra for sample 1. Gap-modes are indicated by arrows.

find any TA corresponding to the 19.3 cm^{-1} line. In order to further explain this result, we considered the model for acoustic phonon Raman scattering described in the previous section to calculate the spectra. The numerical calculation of (14) was performed for the complete system with cap, superlattice and substrate. The substrate was assumed to be about 300 nm thick. The contribution of the substrate was included to quantitatively describe the intensity of the features around 4 cm^{-1}, in which the Si Brillouin scattering adds up to the folded doublets. The calculated spectra were convoluted, with a gaussian simulating the instrumental resolution. The result of this calculation for sample 1 is given as dotted curves in Fig. 3. It can be seen that the experiment is accounted for by our model in detail, including the peak at 19.3 cm^{-1} . In this calculation, fixed values for the Si parameters were taken as $\rho_1 = 2.33$ g/cm^3 and $\vartheta_1 = 8.43 \times 10^5$ cm/s. The structural parameters used are given in Table 1. The complex index of refraction, $n_j = \eta_i + i\kappa_i$ with $j = 1, 2$, obtained from previously published data[25], are listed in Table 2 for the purpose of reference. The alloy layer parameters, ρ_2 and ϑ_2, were taken to be adjustable. The values obtained through this fitting are $\rho_2 = 3.50$ g/cm^3 and $\vartheta_2 = 6.60 \times 10^5$ cm/s. The relative intensities were reproduced by taking $P = P_1/P_2$ as adjustable. The best fit was obtained with $P_{514.5\,nm} = 2.78 + 4.16i$ and $P_{496.5\,nm} = 1.91 + 4.62i$. The vibrational dynamics isolated can be analyzed with the help of the projected density of states. A plot of this function for sample 1 is given in Fig. 4 . The dominant structures in these profiles occur in positions corresponding to the gaps in the dispersion relation of the ideal infinite superlattice. The features corresponding to the alternated zone edge and zone center modes are indicated in Fig. 4 by E_j and C_j , j = 1, 2,..., respectively. Of particular interest is the state labeled E_3 in this plot. The inset of Fig. 4 is an amplification showing that E_3 occurs at $\omega = 19.3$ cm^{-1}, in perfect coincidence with the observed gap-mode. This coincidence indicates that the gap-mode appears as a vibration of the superlattice. The precise nature of this vibration will be discussed later on. It is interesting to note that the PDOS has structures which do not give rise to peaks in the experimental spectra. This is the case of the features labeled C_1 in Fig. 4, in positions corresponding to very weak peaks in the calculated spectra of Fig. 3, which do not appear as peaks in the experimental spectra. The reason is that the electromagnetic effect is q dependent, and the probe is too close to the mini zone edge to reveal structures from the zone center. Our model otherwise produces an excellent description of the experiment.

Similar results were obtained for another superlattice with different parameters, listed as sample 2 in Table 1. Figure 5 shows a comparison between the results of the experiment (solid lines) and the theoretical approach of this work (dotted lines). It should be noted that the gap mode appears at $\omega = 14.8$ cm^{-1} for this sample. The probing wave vectors in this case are $q_{514.5nm} = 0.895\ q_{mz}$ and $q_{496.5\,nm} = 0.935\ q_{mz}$. Very good agreement with the experimental results was observed for the complete frequency range studied, except for the gap mode. The intensity predicted for this gap mode greatly surpassed the observed value. The theoretical peak positions were adjusted to the experimental ones by assuming d_c to be an additional parameter to ρ_2 and ϑ_2. The best fit yielded $d_c = 1.5$ nm. The corresponding values for density and sound velocity are $\rho_2 = 4.05$ g/cm^3 and $\vartheta_2 = 6.10$ cm/s. Note that a thin cap layer does have a marked effect on the vibrational properties of the gap mode. For a fraction of a nm cap thickness variation, the gap mode

Table 2. Optical constant values. Index 1 is relative to the pure element layer, and 2 to the alloy layer.

sample	η_1	κ_1	η_2	κ_2
		$\lambda = 514.5$ nm		
1	4.272	0.014	4.799	0.255
2	4.272	0.014	4.908	0.355
3	4.050	2.585	5.500	1.247
		$\lambda = 496.5$ nm		
1	4.367	0.016	4.997	0.350
2	4.367	0.016	5.083	0.499

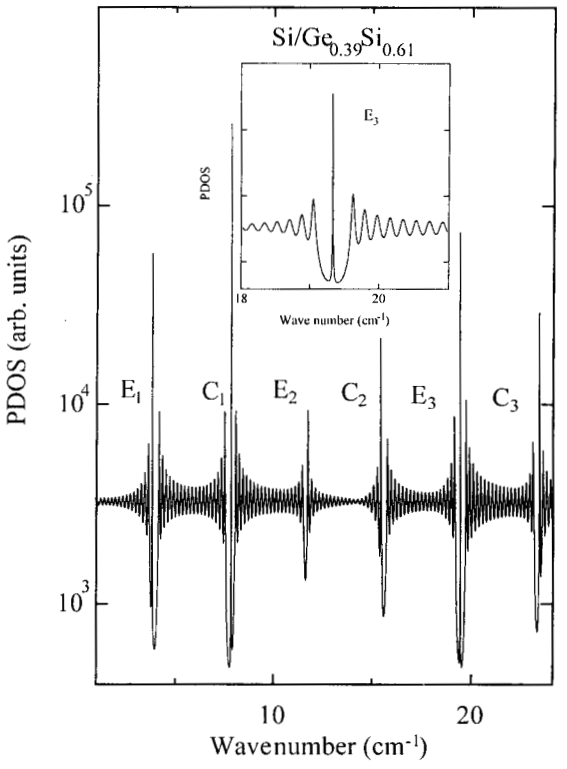

Figure 4. The projected density of states for sample 1. The inset displays the phonon state corresponding to the observed gap mode.

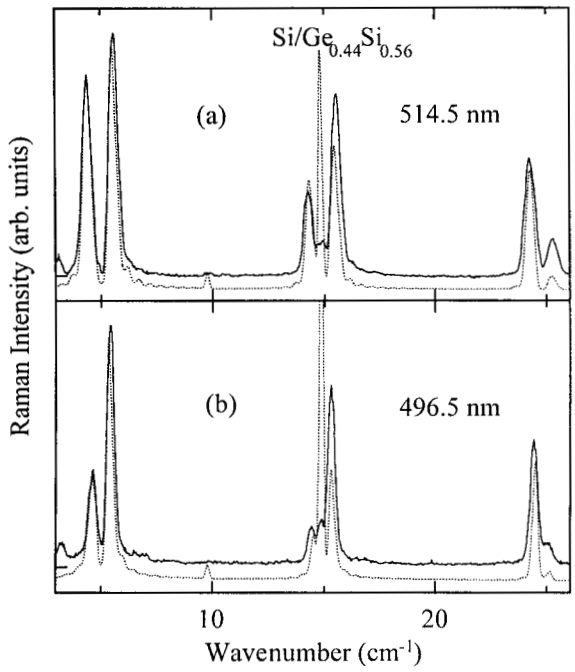

Figure 5. A comparison of measured (solid line) and calculated (dots) spectra for sample 2.

spans the whole acoustic gap, while the other features remain practically unchanged in frequency. The relative intensities were accounted for with P = 4.0i for both excitation wavelengths. Many other combinations of parameters attempted were ineffective in reproducing the spectra. In order to obtain a better description for this mode, we modified the interfaces by allowing a thickness fluctuation of ± 0.25 nm between different layers, but keeping the period fixed. This had the effect of giving a much lower calculated intensity to the gap mode. Although the comparison needs further improvements, it points to the fact that the gap modes are dependent on the perfection of interfaces within the precision of a fluctuation of 2 monolayer per period. This result suggests that perfect interfaces should lead to the observation of gap modes that are even stronger than the usually dominant structures of the folded doublets.

The use of the photoelastic coefficient as two free parameters (real and imaginary parts) allows for a good reproduction of the relative intensities of the various features observed in the experimental spectra. Since the calculated spectra are very sensitive to these quantities, significant information on the acoustic-optic constants of these materials could be deduced from a systematic study of various samples with different alloy compositions and layer thicknesses.

In various Raman studies plausible arguments for the appearance of gap modes are given. This kind of mode was reported in the theoretical studies of transmission through ABA staked superlattices and in double-barrier systems[11,12]. It has been pointed out in refs. 11 and 12, that sharp features within the dip in transmission were highly dependent on the characteristics of the system under study. As a consequence of those observations, a belief was established that the features appear inside the acoustic gap only if the superlattice structure is designed to match the special conditions for constructive interference of elastic waves[11,12]. In a previous publication[24], the appearance of peaks inside the mini-gaps are interpreted as surface modes arising from the creation of the surface of the infinite superlattice. However, no explanation for the physical origin of these modes has been proposed so far. We next propose a mechanism for Raman scattering producing the modes inside the dispersion gaps. We first show that the gap-mode properties are obtained from the first principles applied to a single bilayer system. We show that these modes are not necessarily localized at the surface, let alone when the acoustic impedances of the layers do not differ appreciably. We also point to the important role of the interaction with the substrate.

We chose to discuss a simple system that has many properties in common with superlattices: a diatomic molecule for which the atomic masses obey the relation $m_A < m_B$ [26]. The frequency of vibration of this system is $\omega = \sqrt{k/u}$, where k is the effective force constant and u the reduced mass. Since the center of the mass of the molecule is at rest, the ratio of the vibrational amplitudes of the two atoms is equal to the inverse ratio of the two masses ($R = m_A/m_B$). A linear chain comprising N diatomic molecules with nearest-neighbor interaction has 2 N-1 longitudinal modes. The frequency of the N^{th} mode of the chain is the same as the frequency of the diatomic molecule, ω. This frequency lies in the gap between the acoustic and optical branches. This mode is peculiar because its displacement amplitude decreases with the position of the atoms in the chain, according to the scheme: 1, -R; -R, R^2; R^2, $-R^3$; ..., for the positions A_1, B_1; A_2, B_2; A_3, B_3;..., respectively. Note that for this mode, atoms B_i and A_{i+1} have the same displacement, so that the spring between them is unstrained; the individual AB molecules are mechanically uncoupled. Because the inequality $R < 1$ holds for the decay, localization occurs at the side of the chain ending with the light atom. The localization length can be written in the form $L = a/\ln(1/R)$, with a being the interatomic distance. The properties of this gap mode, referred to as the optical surface mode in Wallis' approach[26], are usually determined by introducing the infinite or cyclic chain model. The surface arises by cutting the cyclic chain, thus decreasing the normal mode frequencies and causing the lowest optical mode to drop down into the gap. Although this approach is traditional, it fails to disclose the nature of the localized modes. Our treatment differs from this in the

sense that the molecule is taken as the unit cell of the chain. It so happens that the vibrational mode of the molecule is the very gap mode of the chain. Also the degree of localization of this mode is calculated by just considering the single molecule.

In what follows we emphasize the appealing similarity between the chain and a free-standing superlattice (FSSL). For the latter, the unit cell is a bilayer system of different constituents. It is possible to obtain the gap mode frequencies of the FSSL by considering only the equation of motion and the boundary conditions in one single unit cell. This will be done next using the elastic continuum approximation. The equation of motion for the unit cell is solved by imposing free stress conditions on the two surfaces and the continuity equation for amplitude and stress at the layer interface. For a fixed value of the relative acoustic impedance we find a discrete set of frequencies, ω_i, which satisfies the boundary conditions at the surfaces, given by:

$$Z \tan\left(\frac{\omega_i d_1}{\vartheta_1}\right) = -\tan\left(\frac{\omega_i d_2}{\vartheta_2}\right) \quad (16)$$

A calculation using this equation gives the frequency values listed in Table 3, up to the order i = 20, for a bilayer $Si/Ge_{0.44}Ge_{0.56}$ with thicknesses of those in sample 2 listed in Table 1, taken as an example here. The numbers for densities and velocities were taken as the previous values found for sample 2. These frequencies, ω_i, lie inside the acoustic gaps of a superlattice constructed with infinite repetitions of the $Si/Ge_{0.44}Ge_{0.56}$ unit cell. An illustration of the displacement amplitude of a gap mode for the described Si/GeSi-based system is shown in Fig. 6 as a function of the position in the superlattice, given in terms of the period. The order i = 10 was chosen for the sake of clarity. The inset represents the same illustration for a single unit cell. It is clear in the inset that the decay occurs at the interface. It should also be noted that the pattern corresponding to a FSSL with N periods is obtained by N repetitions with scaled amplitudes of the pattern for the unit cell. Figure 6 shows that the decay at each interface of a LSSL produces an attenuation of the wave. The evaluation of the decay corresponding to each frequency is accomplished by using the same procedure as before, and yields the following equation:

$$R_i = \left[\cos^2\left(\frac{\omega_i d_1}{\vartheta_1}\right) + Z^2 \sin^2\left(\frac{\omega_i d_1}{\vartheta_1}\right)\right]^{1/2} \quad (17)$$

An interesting point to stress is that the decay is greater for lower values of the factor R_i, its value being restricted to the range $Z \leq R_i \leq 1$. Actually, the R_i value is highly sensitive to the phase of the wave at the interface. If the phase is such that it produces a maximum of the displacement amplitude at the interface, then there is no attenuation of the wave and $R_i = 1$. The other extreme value is $R_i = Z$, corresponding to the maximum attenuation. In the latter situation the displacement amplitude is zero at the interface. For our particular example, the R_i values are listed in Table 3. In order to give a measure of the attenuation of the waves it is useful to define a localization length for the

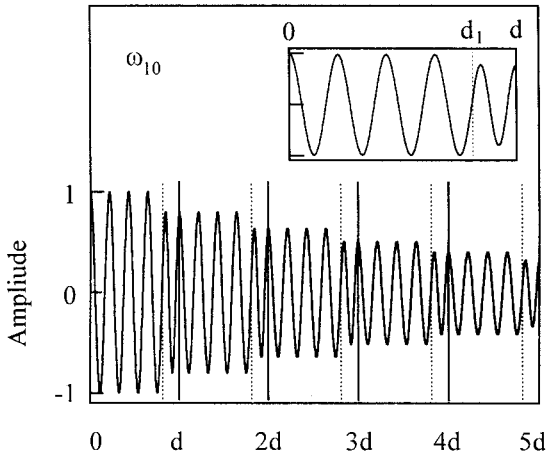

Figure 6. The displacement amplitude for the tenth gap mode of a free-standing superlattice constructed with repetitions of the $Si/Ge_{0.44}Si_{0.56}$ unit cell, with d_1 = 21.5 nm and d_2 = 5.0 nm. The inset gives the displacement amplitude for the single unit cell.

Table 3. Frequencies of normal modes of the $Si/Ge_{0.44}Si_{0.56}$, d_1 = 21.5 nm, d_2 = 5.0 nm unit cell, and parameters calculated for this system, according to the description given in the text.

No.	ω (cm^{-1})	R_i	L_i (d)
1	4.77	0.889	4.3
2	9.88	0.795	2.2
3	15.02	0.876	3.8
4	19.83	0.999	384.4
5	24.57	0.903	4.9
6	29.65	0.796	2.2
7	34.81	0.864	3.4
8	39.65	0.995	106.1
9	44.37	0.917	5.8
10	49.42	0.799	2.2
11	54.59	0.852	3.1
12	59.48	0.989	46.5
13	64.18	0.931	7.0
14	69.19	0.803	2.3
15	74.37	0.842	2.9
16	79.3	0.982	26.9
17	83.99	0.944	8.8
18	88.96	0.808	2.3
19	94.15	0.832	2.7
20	99.12	0.972	17.5

superlattice, similar to the localization length of the molecule previously described:

$$L_i = \frac{d}{2\ln(1/R_i)} \tag{18}$$

For a superlattice constructed with the previously described $Si/Ge_{0.44}Ge_{0.56}$ unit cell, we have the localization lengths listed in Table 3. The numbers are given in terms of the period, d.

We next attempt to establish a criterion to classify the modes according to the wave attenuation from the surface. The length scales with which the localization length can be compared are the vibrational wavelength, the thickness of the superlattice, and the light wavelength. As the latter are the most relevant in light scattering measurements, the modes have a surface character if localized typically within a wavelength from the surface. Adopting this concept, generally accepted by spectroscopists, only those modes with $L_i << \lambda/n$, n being the refraction index of the medium, are surface modes. For the example selected here, the criterion is $L_i << 4$ periods. The analysis of the L_i values of Table 3 shows that half the modes conform to this criterion and have surface character. The other half, on the other hand, cannot be described as surface modes, because for them $L_i > 4$ periods. It should be mentioned at this point in our discussion that for the mode of index i = 4, the magnitude of the localization length has a strikingly high value (L_4 = 384 d). Therefore, the mode is extended throughout any real superlattice based on the $Si/Ge_{0.44}Ge_{0.56}$ unit cell of this study. From the above discussion we conclude that the gap modes are better interpreted as the modes of the single bilayer, rather than surface modes as proposed in a previous publication[24].

The second point we would like to emphasize is the existence of the interaction of the substrate with the superlattice. In order to clarify this point we will examine the PDOS of a single unit cell plus substrate system and a N = 4 superlattice of the same unit cell plus substrate. The results are shown in Fig. 7. Vertical dashed lines in this figure were drawn for the discrete set of frequencies of the free-standing unit cell. It should be noted that the coupling with substrate significantly contributes to the PDOS, not merely by transforming a discrete into a continuous function of energy, but especially because it accounts for the characteristic patterns of each system in question. The importance of the interaction with the substrate can also be evaluated by observing the shifts, broadening, and intensity distribution among the features of the PDOS. To better appreciate the effects of the presence of a substrate we included in Fig. 7 the function R(ω) for the $Si/Ge_{0.44}Ge_{0.56}$ unit cell of this context. The maximum height in the range of energy displayed in Fig. 7 corresponds to the mode with ω_2 = 9.88 cm^{-1}, for which R is the value closest to $R_{min} = Z$, and hence

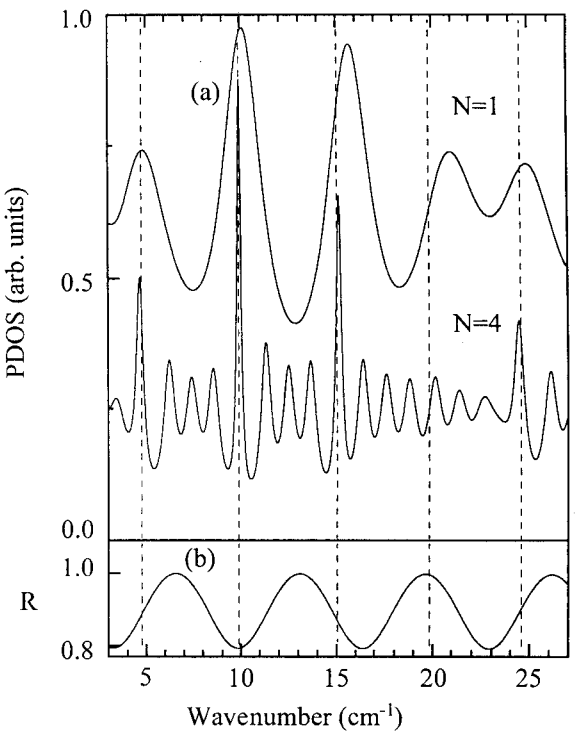

Figure 7. (a) The PDOS for a bilayer and for a N = 4 FSSL coupled to a substrate for the systems described in the text. The dashed lines are the energies of the normal modes of the bilayer system. (b) The factor R related to the localization of the waves.

to the strongest localized mode among those studied here. Considering these arguments it is possible to infer that the interaction of the discrete states of the FSSL with the continuum density of states of the substrate is essential for describing the gap mode properties.

In summary, it is shown in this section that the characteristic frequencies and displacement amplitudes of the gap modes of a FSSL with N periods are determined by the single bilayer. Also, it is shown that the interaction with the substrate is responsible for the broadening and shift of the features in the PDOS corresponding to those modes, as should occur by any additional structure of a real superlattice as in the case of a cap layer. We furnish a criterion based on localization length to classify the modes. The classification of the modes for the example selected here demonstrates that the term, "surface mode", is not always appropriate for describing the gap modes of real systems.

Absorption effect

In this section we present a direct observation of the minizone edge gaps in the dispersion relation of longitudinal acoustic (LA) phonons, measured by Raman scattering of strongly absorbing superlattices. The data reveal peculiar features in the spectra which are dips superimposed on broad scattered intensity. It is shown here that these features are made observable provided there exists some process

resulting in the relaxation of crystal momentum conservation along the superlattice axis. Because the green light used as excitation is strongly absorbed by Ge, absorption processes are responsible for the breakdown of momentum conservation in the scattering from the Ge-based superlattice used in this work.

The low frequency Raman spectra from the $Ge/Ge_{0.72}Si_{0.28}$ superlattice described in Table 1 and its substrate are displayed in Fig. 8. The substrate spectrum, the lower curve in Fig. 8, shows broad bands centered at frequencies $\omega = \pm 3.27$ cm^{-1}. The superlattice spectrum consists of similar broad bands, but for the additional dips in intensity. The appearance of dips as Stokes and anti-Stokes components shows that these features correspond to the inelastic scattering. In order to get a better understanding of the subject, we compare the superlattice and the bulk scattering. The latter contrasts with the standard Brillouin spectra for bulk materials in the sense that the peaks are broad. This broadening has been previously described in terms of the relaxation of crystal momentum conservation, including a precise formalism to account for this effect[1-3]. It is worth rewriting some of the fundamental equations that give a useful physical picture of the origin of the broadening. The high extinction coefficient of Ge is responsible for the scattering volume being restricted perpendicular to the sample surface. In this case, the scattered intensity has to be calculated by means of a complex wave vector transfer, $\mathbf{K} = \mathbf{K'} + i\mathbf{K''}$. The calculation carried out for the particular simple backscattering configuration, yielded the scattered power given by[27]:

$$\frac{dP}{d\omega} \approx \frac{1}{(q - K')^2 + K''^2} \approx \frac{1}{(q/k_0 - 2\eta)^2 - (2\kappa)^2} \qquad (19)$$

with $n = \eta + i\kappa$ being the complex refractive index, and k_0 the vacuum wave vector of the light. Eq. 19 shows that for absorbing materials, excitation with the wave vector within a range of $\Delta q \sim K''$ around the value $q = K'$ may scatter light. Although the spectra in Ref. 27 have been better analyzed by assuming an asymmetric line shape instead of a Lorentzian one, the broadening is explained in a much simpler manner using the above equation. The broad band peaks at the position of the longitudinal phonons. Also, the line shape observed in Fig. 8 is symmetric enough to infer that transverse phonons do not produce a noticeable contribution. The broad bands from the scattering of (111)-Ge surfaces, in contrast, peak at ~±2cm^{-1} and have an asymmetric line shape on the side of higher energies corresponding to the allowance of the longitudinal component, in addition to the major transverse contribution to the scattering. The comparison of the spectra from the superlattice and bulk shows a coincidence in both peak position and line

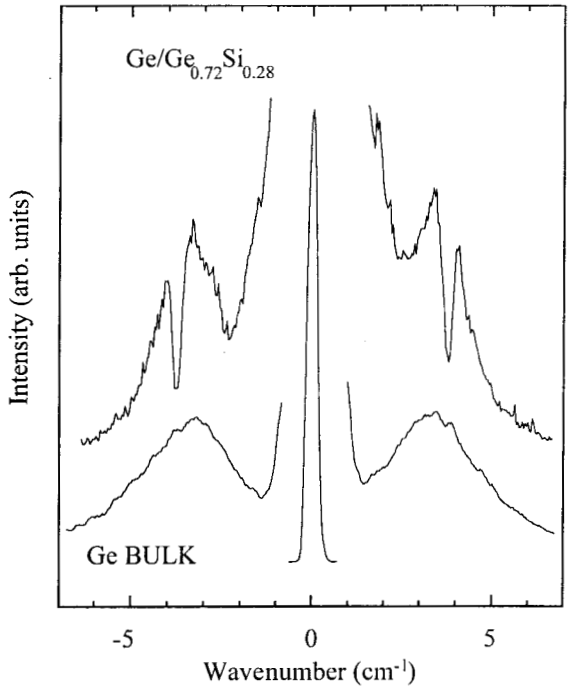

Figure 8. Raman spectra for the $Ge/Ge_{0.72}Si_{0.26}$ superlattice and its substrate.

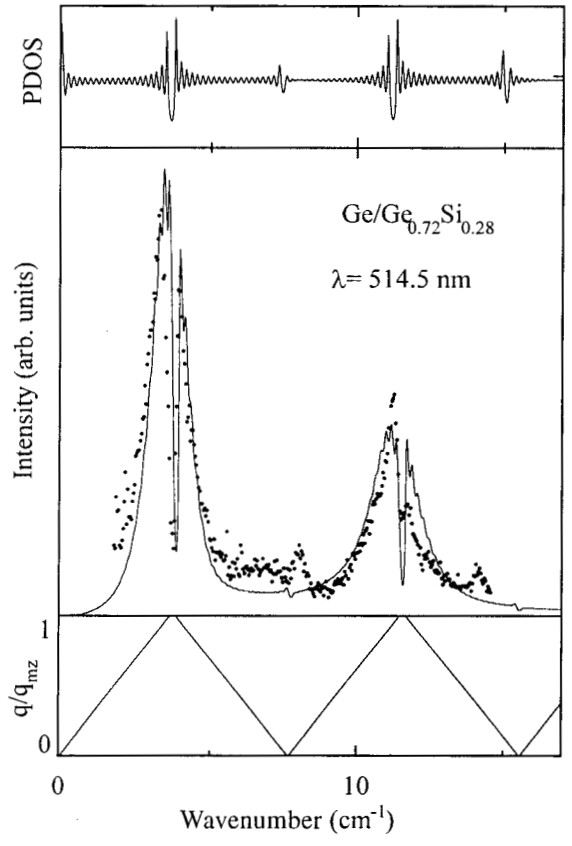

Figure 9. A comparision of measured (solid line) and calculated (dots) Raman spectra. The upper curve is the PDOS and the lower curve is the dispersion relation.

shape thus, indicating the q-vector to be along the superlattice axis.

In order to investigate the intensity anomalies more closely we analyze the Raman spectrum extended to higher orders of folding. Figure 8 shows the experimental curve (dots) together with the result of a numerical calculation (solid line) performed using the approach previously described. The dispersion relation for longitudinal phonons, included at the bottom of Fig. 8, enables a straightforward interpretation of the observed anomalies as corresponding to the acoustic gaps. Because of the fact that the incident radiation probes near the edge of the mini Brillouin zone, the structures appear only at the edge gaps. The zone-center gap manifests as an s-like shape in the calculated spectrum with nearly negligible intensity. In the measured spectrum they are not liable to appear, being covered by the noise background. The calculation was performed using the optical constants listed in Table 1 for sample 3, with the values $\rho_1 = 5.36$ g/cm^3 and $\vartheta_1 = 4.91 \times 10^5$ cm/s as the Ge parameters. The modeling of the experimental spectrum was obtained with the parameters $\rho_2 = 4.45$ g/cm^3 and $\vartheta_2 = 5.60 \times 10^5$ cm/s for the alloy layer. This model also depended on the relative acoustic-optic parameter P =-1.53 - 1.29i.

In conclusion, the Raman scattering of a highly absorbent superlattice is a peculiar spectrum exhibiting pronounced dips superimposed on broad bands. The broad band scattering is due to the spread of wave vector values along the growth direction. The dips were assigned to the acoustic gaps by comparison with the dispersion relation of longitudinal phonons. This is a firsthand observation of the gaps occurring at the mini zone edge. Previous measurements are limited to showing evidence of internal gaps which result from the mixing of longitudinal and transverse waves.

Modulation of the PDOS

The projected density of states is shown in Fig. 2 for several superlattices. The case of a short period superlattice is convenient for the present discussion because its branches are wider along the energy axis of the dispersion relation. This causes the details in the PDOS to be observable in the scattered intensities. To illustrate this situation we chose the Ge_5Si_5 superlattice, grown on a (001) Si substrate (sample 4 in Table 1). For this sample the relation $qd << 1$ holds and the phase of the exciting electric field is practically constant over a Ge_5Si_5 layer. Furthermore, by neglecting long range effects and assuming that P depends on the local properties only, a single effective value of the acoustic-optic coefficient can be considered for both layers. We took this value to be P(z) = 1 for the 145 periods in our calculation. Figure 9 displays the results for experimental (dots) and calculated (solid line) spectra in the case of two excitation lines. The experimental spectra show the periodic modulation superimposed on the Brillouin line. These structures are due to the finite size of the superlattice and reflect the corresponding modulation of the PDOS, as shown in the inset of Fig. 10. The separation between any two successive peaks depends on the vibrational dynamics, so that it is the same for both excitations. Since the energy separation is given by $\Delta\omega = (\vartheta\pi)/(Nd)$, the mean velocity of sound can be obtained. We measured $\Delta\omega = 0.46$ cm^{-1} and calculated $\vartheta = 5.6 \times 10^5$ cm/s from this value. This number was used as input for our computational procedure. The layer thicknesses used were the values listed in Table 1, and the density and velocity of sound were taken as the nominal values for Si and Ge. Because the sample is a symmetrically strained superlattice[28], the optical constants of bulk unstrained material could not be considered. In spite of this limitation we could define the intensity profiles by assuming an effective refraction index for both layers and considering it as a parameter. The real and imaginary parts of n play distinct roles in our calculation. The real part determines the center of the Brillouin peak, whereas the imaginary part determines the overall line width. The fitting yielded $\langle n \rangle_{514.5\ nm} = 6.35 + 0.48$ i and $\langle n \rangle_{496.5\ nm} = 6.45 + 0.67$i . While the imaginary parts fit the extrapolated values from published data for bulk $Ge_{0.5}Si_{0.5}$ compounds very well, the real parts are larger than the corresponding bulk

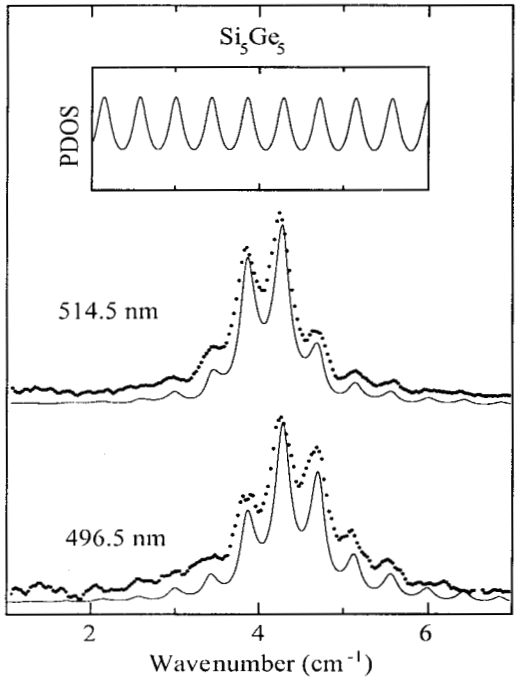

Figure 10. Experimental (dots) and calculated (solid lines) Brillouin spectra for a Ge_5Si_5 superlattice with N = 145 periods. The inset gives the corresponding PDOS.

alloy values. At first, one might expect to find the Ge_5Si_5 superlattice parameters to be close to the bulk $Ge_{0.5}Si_{0.5}$ alloy. This is not the case in the present situation. The crystals in the few constituent monolayers are strained in such a way as to significantly modify the electronic band structure[29]. Actually, the band structure and the dielectric response, in turn, have been found to be very sensitive to n and m in short-period Ge_nSi_m strained-layer superlattices. Considering that we are probing at 2.4-2.5 eV, where the onset of the strong absorption occurs, we expect a maximum for the real part of the dielectric constant at approximately that energy. As a consequence, the index of refraction should be a value between the maxima of that obtained for bulk Si and Ge. This is precisely what happens with our data. For instance, we obtained $\eta \sim 6.4$, whereas η_{max} is 7.0 and 5.5 for Si and Ge, respectively[30].

Satellite lines around the main folded phonon peaks had been previously interpreted in terms of interference between the acoustic phonon waves confined in the whole superlattice and the folded phonon waves[9].

Conclusion

Superlattice crystals have an artificial period, *d*, in the direction perpendicular to the layers, which produces a backfolding of the acoustic phonon dispersion branches onto a reduced mini Brillouin zone. As a consequence, doublets of folded acoustic phonons are observed in high resolution Raman spectra. Additional features, apart from the folded phonon doublets, have also been observed, but could not have been analyzed with existing theory of the past few years. We developed a model for the Raman scattering by acoustic phonons capable of reproducing the experimental profile in detail, including the relative intensities of the doublet lines and extra features. In this model the phonons were treated as elastic waves of a continuum. The wave equation was solved with appropriate boundary conditions at each interface using the transfer matrix method. In order to model the superlattice of a finite size, a numerical calculation was performed where the complete system, superlattice, cap layer, and substrate were considered. Absorption of light was included through the imaginary part of the refraction index. This was found to be particularly important for describing line shapes for highly absorbent materials. The acoustc-optic parameters were taken as adjustable.

Two different superlattices in a series of Si/Si_xGe_{1-x} superlattices with varying layer thickness and composition were experimentally investigated. The Raman spectra of those superlattices reveal peculiar features, in addition to the allowed doublet lines. These features are unusual, as they occur in a frequency range where the dispersion relations have gaps. The modes in the middle of the gaps are shown to have frequency characteristics of the bilayer system taken as the unit cell of the superlattice. Some of these modes are localized if the acoustic impedances of the layers differ appreciably. A criterion is proposed for classifying the modes according to their localization length. Apart from the gap mode intensity the comparison of experiment with theory for this kind of superlattice shows excellent agreement. In order to better describe these modes, we modified our model by allowing a thickness fluctuation between different layers on the order of 0.25 nm, keeping the period fixed. This had the effect of giving a much improved agreement between theory and experimental profile. Although the model needs further improvement, it points to the usefulness of our study in determining interface defects. We present results in more absorbing systems, such as the Ge-based superlattices. Results from such systems allowed for the direct observation of the mini zone edge gaps in the dispersion relation of pure longitudinal acoustic phonons. The Raman spectrum of a Ge_nSi_m superlattice, where n, m indicate the number of monolayer in the alternating layers, shows the Brillouin peak superimposed on by a marked modulation. The structures reflect the corresponding modulation in the density of states calculated for the superlattice with the appropriate numerical values of the parameters. The suitability of the calculation for modeling these systems is demonstrated.

From the study of Raman scattering of folded phonons, several properties such as sound velocities, optical constants, phonon dispersion and elasto-optic constants for the constituent materials of the superlattice can be determined.

Acknowledgments

We thank financial support from Conselho Nacional de Desenvolvimento Científico e Tecnológico (CNPq), Fundação de Amparo à Pesquisa do Estado de São Paulo (FAPESP), and Fundo de Apoio ao Ensino e Pesquisa (FAEP/UNICAMP).

References

1. Ruf, T.; Belitoky, V.I.; Spitzer, J.; Sapega, V.F.; Cardona, M.; Ploog, K. *Phys. Rev. Lett.* **1993**, *71*, 3035.
2. Sapega, V.F.; Belitoky, V.I.; Ruf, T.; Fuchs, H.D.; Cardona M.; Ploog, K. *Phys. Rev. B* **1992**, *46*, 16 005.
3. Ruf, T.; Sapega, V.F.; Belitoky, V.I.; Cardona, M.; Ploog, K. *Phys. Rev. B* **1994**, *50*, 1 792.
4. Talochkin, A.B.; Markov, V.A.; Neizvestnyi, I.G.; Pchelyakov, O.P.; Sinyukov, M.P.; Stenin, S.I. *Pis'ma Zh. Eksp. Teor. Fiz.* **1989**, *50*, 21 [*JETP LETT.* **1989**, *50*, 24].
5. Lockwood D.J.; Young J.F. In *Light Scattering from Semiconductor Structures and Superlattices* (Plenum: New York 1991).
6. Lemos, V.; Pilla, O.; Montagna. M.; Benassi, P.; Fontana, A.; de Souza, C.F.; Carvalho, Jr., W. *Braz. J. Phys.* **1994**, *24*, 214.

7. Pilla, O.; Lemos, V.; Montagna, M. *Phys. Rev. B* **1994**, *50*, 11845.
8. Lemos, V.; Pilla, O.; Montagna, M.; de Souza, C.F. *Superlattice and Microstruture* **1995**, *17*, 51.
9. Zang, P.X.; Lockwood, D.J.; Baribeau, J.-M. *Appl. Phys. Lett.* **1993**, *62*, 267.
10. He, J.; Djafari-Rouhani, B.; Sapriel, J. *Phys. Rev. B* **1988**, *37*, 4 086.
11. Tamura, S.; Hurley, D.C.; Wolfe, J.P. *Phys. Rev. B* **1988**, *38*, 1 427.
12. Misuno, S.; Tamura, S. *Phys. Rev. B* **1992**, *45*, 13 423; *ibid.* **1992**, 734.
13. Ovsyuk, N.N.; Novikov, V.N. *JETP Letters* **1995**, *62*, 647.
14. Knipp, P.A.; Reinecke, T.L. *Phys. Rev. B* **1995**, *52*, 5 923.
15. Y. Talmi, Proc. of SPIE: *Raman and Luminescence Spectroscopy in Technology* **1987**, *822*, 132.
16. Tsang J.C. In: *Light Scattering in Solids,* Edited by Cardona, M.; Güntherodt, G. (Springer: New York 1989) p. 233.
17. Mazzacurati, V.; Benassi P.; Ruocco, G. *J. Phys. E: Sci. Instrum.* **1988**, *21*, 798.
18. Lockwood, D.J.; Dharma-Wardana, M.W.C.; Baribeau, J.-M.; Houghton, D.C. *Phys. Rev. B* **1987**, *35*, 2 243.
19. Jusserand, B.; Cardona, M. In: *Light Scattering in Solids,* Edited by M. Cardona and G. Güntherodt (Springer: New York 1989) p. 49.
20. Hayes, W.; Loudon, R. In: *Scattering of Light by Crystals* (Wiley: New York 1978).
21. Sapriel, J.; Michel, J.C.; Tolédano, J.C.; Vacher, R.; Kervarec, J.; Regreny, A. *Phys. Rev. B* **1983**, *28*, 2 007.
22. Covard, C.; Gant, T.A.; Klein, M.V. *Phys. Rev. B* **1985**, *31*, 2 080.
23. Rytov, S.M. *Soc. Phys. Acoust.* **1956**, *2*, 67.
24. El Boudouti, E.H.; Djafari-Rouani, B.; Khoudifi, E.M.; Dobrzynski, L. *Phys. Rev. B* **1993**, *48*, 10 987.
25. Humlicek, J.; Garriga, M.; Alonso, M.I.; Cardona, M. *J. Appl. Phys.* **1989**, *65*, 2 827.
26. Wallis, R.F. In: *Dynamical Properties of Solids,* Edited by G.K. Horton and A.A. Maradudin (North-Holland: Amsterdam 1975).
27. Sandercock, J.R. In: *Light Scattering in Solids,* Edited by M. Cardona and G. Güntherodt (Springer: New York 1982) p. 173.
28. Kasper, E.; Kibbel, H.; Jorke, H.; Brugger, H.; Fries, E.; Abstreiter, G. *Phys. Rev. B* **1988**, *38*, 3 599.
29. Schmid, U.; Christensen, N.E.; Alouani, M.; Cardona, M. *Phys. Rev. B* **1991**, *43*, 14 597.
30. Landolt-Börnstein Tables, Edited by Madelung, O.; Shulz, M.; Weiss, H. (Springer-Verlag: Berlin 1984) Vol 17b.

FAPESP helped in meeting the publication costs of this article